Crystallization, Reentrant Melting and Resolubilization of Virus Nanoparticles

Roi Asor,[†,‡] Orly Ben-nun-Shaul,[¶] Ariella Oppenheim,[¶] and Uri Raviv[*,†,‡]

†*Institute of Chemistry, The Hebrew university of Jerusalem, Edmond J. Safra Campus, Givat Ram, Jerusalem, 9190401, Israel*

‡*Center for Nanoscience and Nanotechnology, The Hebrew University of Jerusalem, Edmond J. Safra Campus, Givat Ram, Jerusalem, 9190401, Israel*

¶*Department of Haematology, The Hebrew University Faculty of Medicine and Hadassah Medical Organization, Ein Karem, Jerusalem 91120, Israel*

E-mail: uri.raviv@mail.huji.ac.il

Phone: +972-2-6586030. Fax: +972-2-566-0425

1. Validation of the ideal gas approximation for the 10 mM $MgCl_2$ signal

At low resolution, the virus particle can be approximated by a sphere with a radial electron density contrast (with respect to the buffer solution). Any deviation from this approximation is owing to positional correlations between the viruses in the solution (deviation from the ideal gas approximation) that result from either attractive or repulsive interactions. In Figure S1 the low q-range of the signal is shown together with a smooth spherical model for which

the electron density contrast profile is described by the following equation:

$$\Delta\rho\left(r\right)=0.5\left(\Delta\rho_{1}+\sum_{i=1}^{N-1}\left[\left(\Delta\rho_{i+1}-\Delta\rho_{i}\right)\right]\tanh\left[s_{i}\left(r-R_{i}\right)\right]\right) \tag{S1}$$

The index i represents the ith layer in the sphere, with an outer radius, R_i, an electron density contrast,$\Delta\rho_i$, and linked to the subsequent layer, $i+1$, by a slope s_i. $\Delta\rho_N = 0$ and corresponds to the solvent electron density contrast. The form-factor was computed using our analysis program X+ as explained.[1–4]

As at low resolution wt SV40 particles may be considered spherical, we expect that when the solution is ideal (no interparticle interactions) the scattering curve should be similar to the computed red curve in Figure S1. The experimental data is consistent with the computed spherical model down to $q = 0.05\,\mathrm{nm}^{-1}$, suggesting that the interactions between virus particles are relatively weak and therefore can not be detected within the measured q-range.[5] Therefore considering the 10 mM signal as the measured virus form-factor is well justified.

2. Justification of the decoupling approximation with $\beta = 1$

By using the decoupling approximation and setting $\beta = 1$, we could write that the averaged scattering intensity of the virus in the crystalline phase (up to some resolution threshold) by Eq. 4. To justify this approximation and finding the resolution threshold, we modeled the scattering intensity of the virus crystal in two different methods. In the first method, we computed the scattering intensity of the virus capsid (pdb ID 1SVA) using D+ software[6] and multiply the scattering intensity by the orientation averaged intensity of a BCC lattice points with 20 repetitions in each of the three directions and with a lattice vector size of 56.7 nm. This method corresponds to the calculation described in Eq. 4. In the second

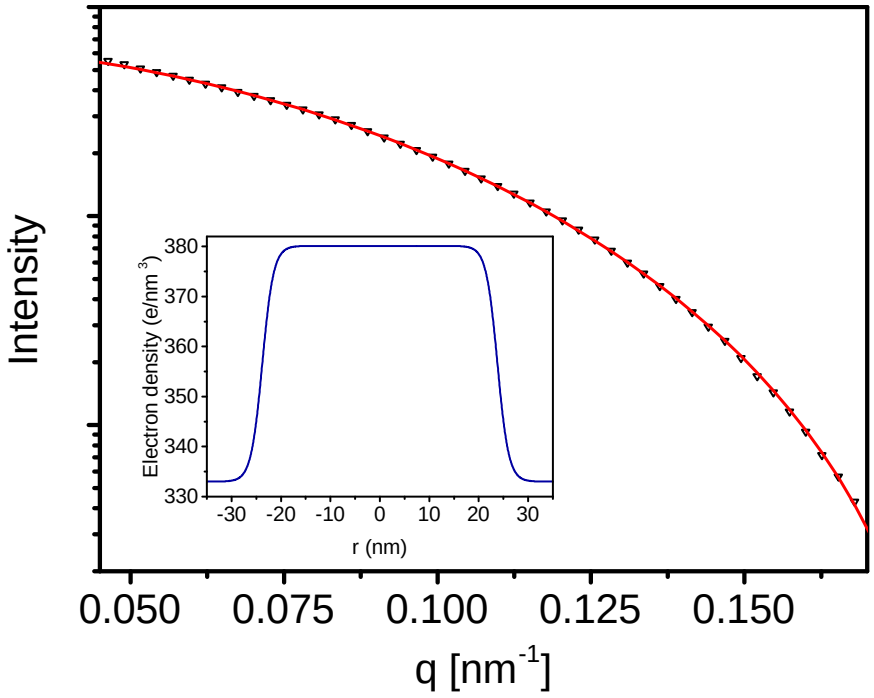

Figure S1: Contribution of interparticle spatial correlations to the azimuthally integrated SAXS intensity when 10 mM $MgCl_2$ were added to wt SV40. Black symbols represent the lower q-range of the experimental scattering intensity curve. The red curve is the computed scattering intensity (using Eq. 1) from a spherical particle with a radial electron density contrast, $\Delta\rho(r)$, shown at the inset and is given by Eq. S1 with $N = 2$, $R_1 = 23.8\,\mathrm{nm}$, $\Delta\rho_1 = 47\,\frac{\mathrm{e}}{\mathrm{nm}^3}$, and $s_1 = 0.4$.

method, we computed the expected scattering intensity based on Eq. 2, using D+ and the same structural parameters. To perform this calculation at atomic resolution (using the crystal structure of the virus as the form factor) one needs to build a lattice containing 20^3 viruses, where each virus contains approximately 10^6 atoms. The calculation can be done with great accuracy and very fast using D+ software that uses a hierarchical algorithm to represent this lattice as explained elsewhere.[6] From the superimposed calculated intensities from these two methods, as shown in Figure S2, it is possible to see that the two computation methods fall one on top of the other up to a q-value somewhere between 0.6 and 0.7 nm^{-1}. $q \approx 0.65\,\mathrm{nm}^{-1}$ corresponds to the inter-pentamers distances. Above this q value, inter-pentamer correlations significantly contribute to the scattering intensity. In this limit the spherical approximation does not hold, hence Eq. 8 can not represent the normalized data correctly.

3. Peak indexing and shape, lattice planes, and phase fitting results

The crystal structure unit cell and indexing of the scattering planes were all fitted using X+ software.[1] The peak positions pattern that was fitted is with excellent agreement with a BCC (Im3m) lattice. To extract the unit cell parameters from the fit, it is possible to represent the BCC lattice symmetry by the primitive basis as shown in Figure S3 and defined by the following three unit vectors:

$$\begin{aligned} \vec{a}_1 &= \frac{a}{2}\left(-\hat{x}+\hat{y}+\hat{z}\right) \\ \vec{a}_2 &= \frac{a}{2}\left(\hat{x}+\hat{y}+\hat{z}\right) \\ \vec{a}_3 &= \frac{a}{2}\left(-\hat{x}-\hat{y}+\hat{z}\right) \end{aligned} \tag{S2}$$

where a is the distance between two vertices of the cube. Usually, it is more convenient to use a different basis, which contains orthogonal vectors. The orthogonal basis can be formed

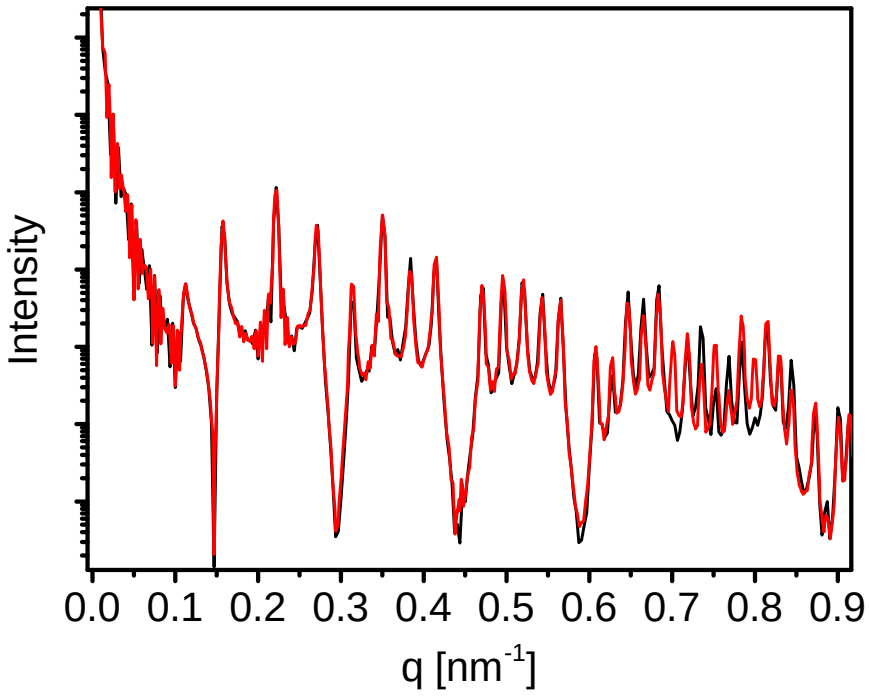

Figure S2: Demonstration for the justification of the spherical approximation using the scattering curve of wt SV40 in 100 mM $MgCl_2$. A BCC lattice with a unit cell vectors size of 56.67 nm and 20 repetition along each direction was calculated using D+ software[6] in two different method. The red curve represent the calculated intensity using Eq. 4 while the black curve represent the expected scatteing intesity of the same lattice but calculated by Eq. 2. As can be seen from the superimposed curves, considerable deviations in the peaks heights start to appear at $q \approx 0.65\,\mathrm{nm}^{-1}$.

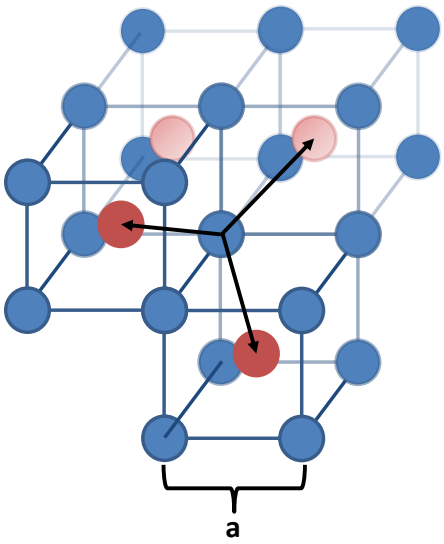

Figure S3: Real space symmetry of body centered cubic (BCC) lattice. Primitive basis for BCC lattice set by the vectors: ($\vec{a}_1, \vec{a}_1$, and $\vec{a}_1$).

by a linear combination of the primitive basis:

$$\begin{aligned}\vec{A}_1 &= -\left(\vec{a}_1 + \vec{a}_3\right) \\ \vec{A}_2 &= \vec{a}_1 + \vec{a}_2 \\ \vec{A}_3 &= \vec{a}_2 + \vec{a}_3.\end{aligned} \tag{S3}$$

When using the orthogonal basis it is necessary to specify an additional translation $\vec{T} = \frac{1}{2}\left(\vec{A}_1 + \vec{A}_2 + \vec{A}_3\right)$, as illustrated in Figure S4.

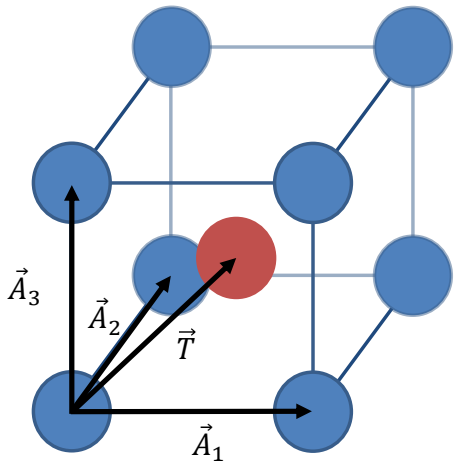

Figure S4: Real space symmetry of a BCC lattice with the orthogonal basis $(\vec{A}_1, \vec{A}_2, \vec{A}_3)$ and the additional translation $\vec{T} = \frac{1}{2}\left(\vec{A}_1 + \vec{A}_2 + \vec{A}_3\right)$

A more intuitive way to describe the crystal symmetry is to define a two components unit cell (as shown in Figure S5), in which the object of interest (in this case wt SV40) has two

positions, set by the following two translation vectors:

$$\begin{aligned} \vec{t}_0 &= \vec{0} \\ \vec{t}_1 &= \frac{a}{2}(1,1,1) \end{aligned} \tag{S4}$$

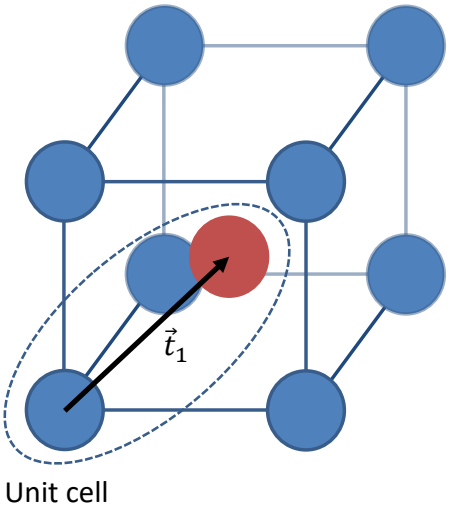

Figure S5: Real space symmetry of BCC lattice with a two component unit cell and the orthogonal basis $(\vec{A}_1, \vec{A}_2, \vec{A}_3)$.

The new unit cell can now be placed into a higher symmetry of a simple cubic lattice. Mathematically, we can define the electron density of wt SV40 crystal by:

$$\rho_{\text{crystal}}(\vec{r}) = \overbrace{\rho_{\text{SV40}}(\vec{r}) \otimes \left(\delta\left(\vec{r}-\vec{t}_0\right) + \delta\left(\vec{r}-\vec{t}_1\right)\right)}^{\text{unit cell}} \otimes \overbrace{\sum_{n_1,n_2,n_3} \delta\left(\vec{r}-\vec{R}_{n_{1,2,3}}\right)}^{\text{simple cubic lattice}} \tag{S5}$$

Where, $\rho_{\text{SV40}}(\vec{r})$ is the 3D electron density profile of SV40 and $\vec{R}_{n_{1,2,3}} \equiv n_1\vec{A}_1 + n_2\vec{A}_2 + n_3\vec{A}_3$

is the set of vectors that describe the cubic lattice with $n_{1,2,3} \in \mathbb{Z}$. The scattering amplitude in reciprocal-space is given by the Fourier transform of the electron density, which is given in real-space. Therefore, the amplitude of wt SV40 crystal is given by: $\mathcal{F}\left\{\rho_{\text{crystal}}\left(\vec{r}\right)\right\}$. Applying the transform on the $3D$ electron density and using the convolution theorem gives,

$$\mathcal{F}\left\{\rho_{\text{crystal}}\left(\vec{r}\right)\right\} = \mathcal{F}_{\text{unit cell}}\left(\vec{q}\right) \times \mathcal{F}_{\text{lattice sum}}\left(\vec{q}\right) \tag{S6}$$

where the unit cell contribution can by written by

$$\mathcal{F}_{\text{unit cell}}\left(\vec{q}\right) = \mathcal{F}_{\text{SV40}}\left(\vec{q}\right)\left(e^{-i\vec{q}\cdot\vec{t}_0} + e^{-i\vec{q}\cdot\vec{t}_1}\right) \tag{S7}$$

and for the BCC lattice sum we get,

$$\mathcal{F}_{\text{lattice sum}}\left(\vec{q}\right) = \sum_{n_1,n_2,n_3} e^{-i\vec{q}\cdot\vec{R}_{n_{1,2,3}}}. \tag{S8}$$

As the real-space lattice can be spanned by a basis of three vectors, the reciprocal-space (or scattering-space) can be spanned by the same number of unit vectors. The relation between the real-space basis and the reciprocal-space basis is given by,

$$\vec{a}_1^{\star} = 2\pi\frac{\vec{a}_2 \times \vec{a}_3}{\vec{a}_1 \cdot (\vec{a}_2 \times \vec{a}_3)}, \vec{a}_2^{\star} = 2\pi\frac{\vec{a}_3 \times \vec{a}_1}{\vec{a}_1 \cdot (\vec{a}_2 \times \vec{a}_3)}, \vec{a}_3^{\star} = 2\pi\frac{\vec{a}_1 \times \vec{a}_2}{\vec{a}_1 \cdot (\vec{a}_2 \times \vec{a}_3)} \tag{S9}$$

where, in this case $\vec{a}_{1,2,3}$ are the lattice vectors of a simple cubic symmetry. According to this definition the two sets of vectors (real and reciprocal) obey the orthogonality condition, $\vec{a}_i^{\star} \cdot \vec{a}_j = \delta_{ij}$ and $|\vec{a}_i^{\star}| = \frac{2\pi}{|\vec{a}_i|}$. Therefore the general reciprocal vector $\vec{q}$ can be define by the linear combination of those three vectors, $\vec{q} = h\vec{a}_1^{\star} + k\vec{a}_2^{\star} + l\vec{a}_3^{\star}$. According to the Laue condition, for large number of repetition along each lattice dimension the sum in Eq. S8 is of the order of unity, where h, k, and l are not integers (because the sum is over a large number of arbitrary phases) and of the order of the number of lattice repetitions when h, k and $l \in \mathbb{Z}$. With this result we can assume that the lattice sum restricts the $\vec{q}$ space into a

set of discrete values with $h, k, l \in \mathbb{Z}$, in which the scattering is non-vanishing (For complete mathematical description the reader is referred to chapters 4 and 5 in ref.[7] or any other book on solid state physics or x-ray scattering).

The scattering amplitude from a crystalline structure can be separated into the scattering owing to the unit-cell electron density and the lattice sum function, describing the symmetry of the macroscopic crystal (Eq. S6). Writing the scattering amplitude of the unit cell with the restriction of the cubic lattice where $\vec{q} = \frac{2\pi}{a}(h, k, l)$ gives the total scattering amplitude,

$$\mathcal{F}(\vec{q}) = \mathcal{F}_{\mathrm{SV40}}(\vec{q})\left(1 + e^{-i\pi(h+k+l)}\right). \tag{S10}$$

The scattering amplitude from a perfect large enough lattice can therefore be written by the followings,

$$\mathcal{F}(\vec{q}) = \begin{cases} 2\mathcal{F}_{\mathrm{SV40}} & \text{if } h+k+l \text{ is even} \\ 0 & \text{if } h+k+l \text{ is odd} \end{cases}. \tag{S11}$$

The scattering intensity is defined as, $I(\vec{q}) = \mathcal{F}(\vec{q})\,\mathcal{F}(\vec{q})^*$. From Eq. S11 we therefore expect that the pattern of peaks positions of the measured structure factor will correspond to the even lattice planes of a simple cubic symmetry with only one free parameter, a. The fitting procedure was performed as described in the Methods section. The indexation of the peaks can be seen in Figure S6 were the signal with the most pronounced structure factor (100 mM $MgCl_2$ with no added NaCl) was chosen to indicate the peaks positions. The peaks are labeled with integers ranging from 1 to 28, each index is assigned to a corresponding lattice plane or a set of lattice planes as appears in Table S1. Table S2 and Table S3 compare the expected peak centers in each $MgCl_2$ concentration (with and without added 0.5 M NaCl) with the fitted values in Figure 2. The absolute value of the difference between the two values is provided as the error.

Table S1: A list of BCC lattice planes that correspond to each one of the scattering correlation peaks, indexed in Figure S6.

Peak number	BCC Lattice planes
1	(1,1,0)
2	(2,0,0)
3	(2,1,1)
4	(2,2,0)
5	(3,1,0)
6	(2,2,2)
7	(3,2,1)
8	(4,0,0)
9	(3,3,0),(4,1,1)
10	(4,2,0)
11	(3,3,2)
12	(4,2,2)
13	(3,4,1),(5,1,0)
14	(5,2,1)
15	(4,4,0)
16	(4,3,3),(5,3,0)
17	(4,4,2),(6,0,0)
18	(5,3,2),(6,1,1)
19	(6,2,0)
20	(5,4,1)
21	(6,2,2)
22	(6,3,1)
23	(4,4,4)
24	(5,4,3),(5,5,0)
25	(6,4,0)
26	(5,5,2),(6,3,3)
27	(6,4,2)
28	(7,3,0)

The list of lattice planes was extracted using X+ software.[1]

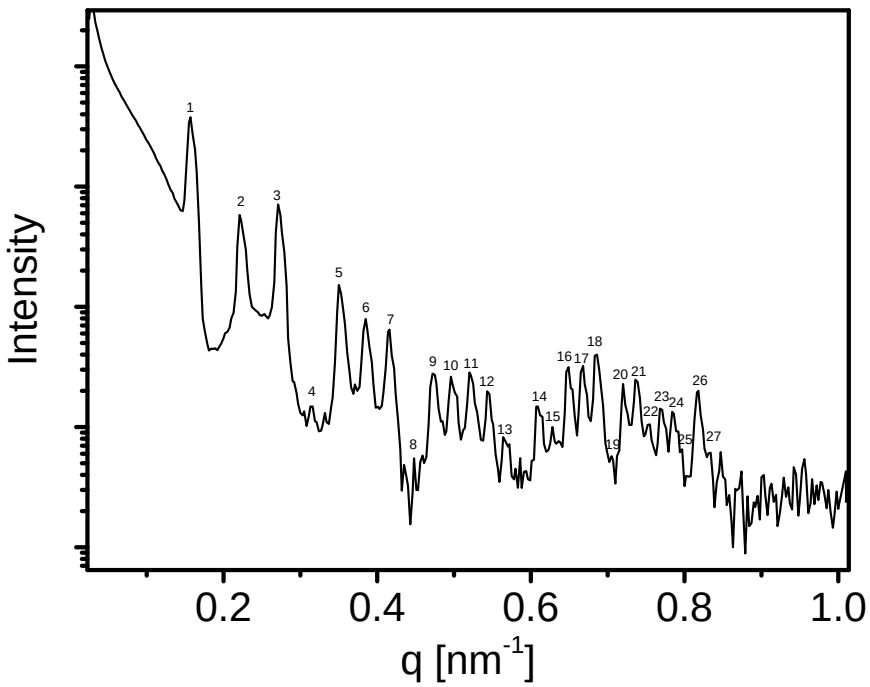

Figure S6: Example for BCC lattice peak assignment obtained for the scattering curve of wt SV40 in 100 mM $MgCl_2$. The associated lattice planes are listed in Table S1.

Table S2: The resultant size of the cubic unit cell vector, a, and peaks positions from fitting the structure factor model presented in Eq. 8 to the scattering data as shown in Figure 2a.

$a = 55.91$nm										
	20 mM		30 mM		50 mM		100 mM		300 mM	
Expected	Fitted	Error	Fitted	Error	Fitted	Error	Fitted	Error	Fitted	Error
0.15894	0.162708	0.003768	0.163445	0.004505	0.163863	0.004923	0.163795	0.004855	0.163568	0.004628
0.224776	0.228388	0.003612	0.226722	0.001946	0.225539	0.000763	0.227324	0.002548	0.22811	0.003334
0.275293	0.276236	0.000943	0.277115	0.001822	0.277701	0.002408	0.277221	0.001928	0.278073	0.00278
0.317881	-	-	0.328529	0.010648	0.320919	0.003038	0.318026	0.000145	0.325872	0.007991
0.355401	-	-	0.355226	0.000175	0.354354	0.001047	0.357048	0.001647	0.354125	0.001276
0.389323	-	-	0.389305	0.000018	0.388899	0.000424	0.390504	0.001181	0.387738	0.001585
0.420516	-	-	0.420934	0.000418	0.420867	0.000351	0.420888	0.000372	0.420261	0.000255
0.476821	-	-	0.473825	0.002996	0.4752	0.001621	0.475045	0.001776	0.475177	0.001644
0.502613	-	-	0.501525	0.001088	0.501663	0.00095	0.500668	0.001945	0.500796	0.001817
0.527145	-	-	0.524529	0.002616	0.525216	0.001929	0.524682	0.002463	0.523545	0.0036
$a = 56.67$nm										
	20 mM		30 mM		50 mM		100 mM		300 mM	
Expected	Fitted	Error	Fitted	Error	Fitted	Error	Fitted	Error	Fitted	Error
0.156796	0.156632	0.000164	0.156646	0.00015	0.156998	0.000202	0.15695	0.000154	0.156752	0.000044
0.221743	0.22232	0.000577	0.221289	0.000454	0.221016	0.000727	0.221284	0.000459	0.221249	0.000494
0.271579	0.270806	0.000773	0.271324	0.000255	0.271508	0.000071	0.271254	0.000325	0.271473	0.000106
0.313593	-	-	0.313637	0.000044	0.313626	0.000033	0.31413	0.000537	0.316348	0.002755
0.350607	-	-	0.350584	0.000023	0.350153	0.000454	0.350568	0.000039	0.349507	0.001100
0.384071	-		0.38418	0.000109	0.383716	0.000355	0.384181	0.00011	0.383255	0.000816
0.414844	-	-	0.41511	0.000266	0.415131	0.000287	0.415119	0.000275	0.414382	0.000462
0.470389	-	-	0.46859	0.001799	0.470269	0.00012	0.470102	0.000287	0.46758	0.002809
0.495834	-	-	0.49626	0.000426	0.49619	0.000356	0.49549	0.000344	0.494851	0.000983
0.520035	-	-	0.521715	0.00168	0.521641	0.001606	0.520343	0.000308	0.519806	0.000229

The expected peaks positions correspond to a BCC (Im3m) symmetry with a unit cell vector $\vec{a}$, the fitted positions correspond to the center of each peak in the data, q_i^*, that was found by fitting Eq. 6. The error is the absolute difference between these two values.

Table S3: The resulting of the cubic unit cell vector size, a, and peaks positions from fitting the structure factor model presented in Eq. 8 to the scattering data as shown in Figure 2b.

$a = 56.4$nm						
	100 mM		300 mM		400 mM	
Expected	Fitted	Error	Fitted	Error	Fitted	Error
0.157582	0.159655	0.002073	0.159545	0.001963	0.159657	0.002075
0.222854	0.222217	0.000637	0.222191	0.000663	0.222252	0.000602
0.272940	0.273477	0.000537	0.273352	0.000412	0.273428	0.000488
0.315164	0.311824	0.00334	0.314116	0.001048	0.311824	0.00334
0.352364	0.351771	0.000593	0.351398	0.000966	0.351771	0.000593
0.385995	0.386147	0.000152	0.385976	0.000019	0.386147	0.000152
0.416922	0.417403	0.000481	0.417919	0.000997	0.417403	0.000481
0.498317	0.496398	0.001919	0.496585	0.001732	0.496398	0.001919
0.522640	0.524229	0.001589	0.524268	0.001628	0.524229	0.001589

Columns are arranged as in Table S2. At each concentration, the expected peak center is compared with the fitted peak center and the difference between the two indicated as the error.

3.1 When no NaCl was added, two crystalline phases coexisted

Figure S7 shows that when no NaCl was added the series of structure-factor line-shapes where asymmetric. We attribute this asymmetry to the fact that two wt SV40 BCC crystalline phases, with slightly different lattice constants, coexisted.

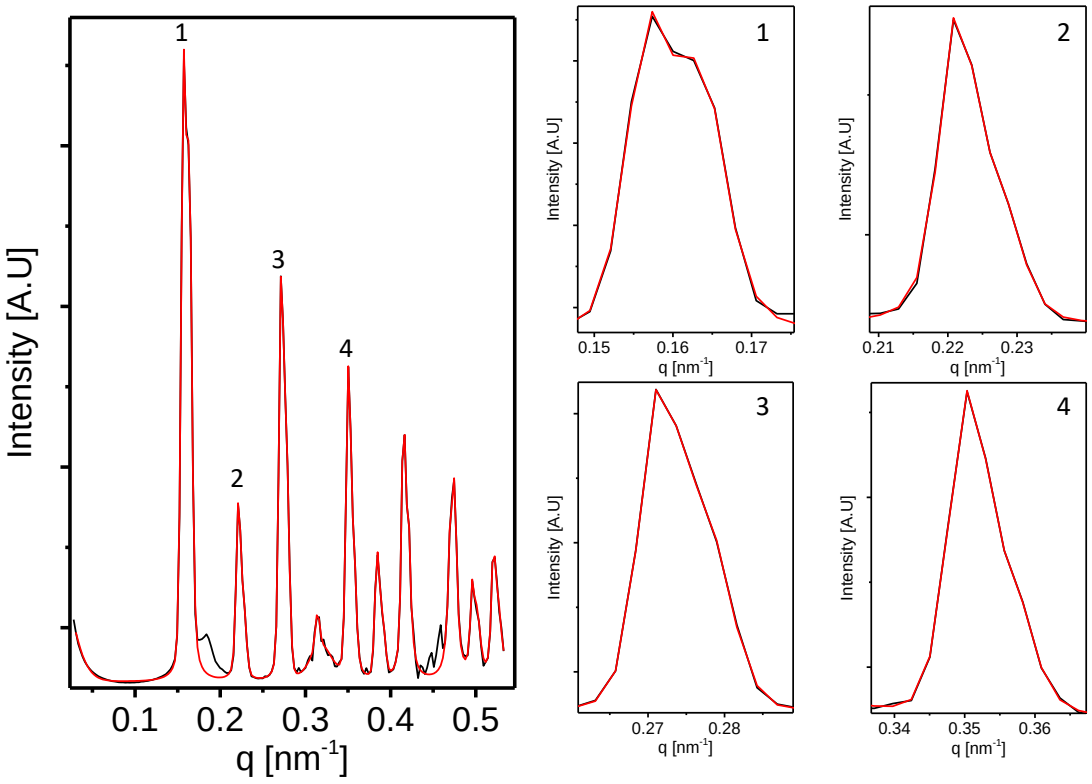

Figure S7: Asymmetric structure-factor peak line-shapes. The large graph on the left shows the normalized structure-factor of wt SV40 in 100 mM $MgCl_2$ solution. The line-shapes of the four enumerated peaks are shown on the right on an expanded scale and reveal a considerable asymmetry. The peaks line-shapes can be reproduced using at least two different BCC crystals, as shown in Table S2.

3.2 Effect of small changes in the form-factor on the structure-factor analysis

The genome of SV40 is a circular ds-DNA that condenses around nucleosemes to form a minichrimosome structure inside the capsid. Earlier works showed that when adding multi-

valent cations, like Mg^{2+} or spermine, to a solution of nucleosome core particles, the particles may condense to form ordered crystalline phases.[8–10] Figure S8 shows that at high and low $MgCl_2$ concentrations, when no crystals formed, the form-factor of wt SV40 has changed. Based on our earlier simulations,[3] we attribute these changes to small changes in the structure of the minichromosome. These changes are mostly seen at the locations of the form-factor minima and maxima. Figure S8 shows that the additional (not modeled) structure-factor peaks and valleys fall exactly at the position of the minima of the form-factor signal. Because the slopes of the curve close to the minima are large, any deviation of the form-factor at these positions can modify the structure-factor in a way that may appear as additional correlation peaks.

4. Electrophoretic mobility measurements

Electrophoretic mobility (EM) measurements were perform using Zetasizer nano ZSP (Malvern) which uses phase analysis light scattering (PALS) for the determination of EM. The measurements were carried out using the diffusion barrier technique to minimize sample degradation near the electrode positions. In this technique, a standard 1 mL zeta cell (1070) was filled with the filtered salt solution from the dialysis beaker of each sample and then 50 μL of the dialyzed virus sample was pipetted directly into the bottom of the cell. All measurements were perform at 25 °C. For the spermine samples, which were in the low conductivity range ($<5\,^{\mathrm{mS}}/_{\mathrm{cm}}$), the automated protocol, which uses a longer application of the steady field at 150 V (a combination of the fast field and slow field reversal), was carried out. In this mode, the results of each measurement was a distribution of the electrophoretic mobility with an average mobility and standard deviation. Each of the data points in Figure S9 is the average and mean standard deviation of three different measurements. The samples that contained $MgCl_2$ above concentration of 20 mM were in the high conductivity range ($>5\,^{\mathrm{mS}}/_{\mathrm{cm}}$). In this range, the voltage was reduced to 40-50 V for the 50 and 100 mM $MgCl_2$ samples and to 10 V

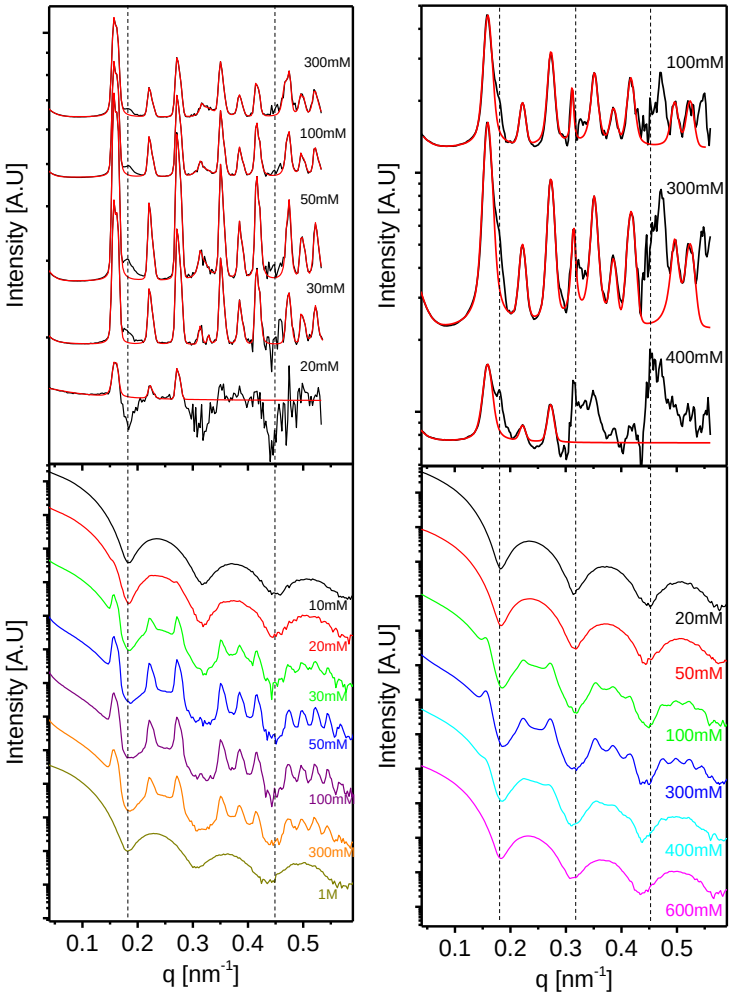

Figure S8: Slight deviation of the form factor relative to the reference form factor may result with artifacts in the normalized signals. The figure demonstrates that the deviations from the fitted structure factor model (red curves in the upper parts of the figure) are positioned exactly at the positions of the minima of the form factor. These positions are the most sensitive to changes in the form factors that result from increasing the $MgCl_2$ concentrations.

for the 500 mM $MgCl_2$ sample. In this range, the measurements where carried out using the monomodal analysis method, which uses the fast field reversal only to minimize degradation of the sample and electrodes. For this analysis method the result of the measurement was only the mean electrophoretic mobility. The presented data points for these conditions are the averages of three different measurements and the errors are the calculated standard deviations. The low $MgCl_2$ concentrations samples (10 and 20 mM) were measured using the same protocol as the spermine samples. At 20 mM $MgCl_2$ the conductivity was equal to 4.5 $^{mS}/_{cm}$, which is close to the high conductivity threshold. In this case, the automated protocol caused degradation of the electrode and therefore the presented data point for this condition corresponds to the first electroporetic mobility measurement.

If we approximate the EM of the virus by Henry's equation[11] for charged spherical colloids as was done previously,[12] we find that the data in Figure S9 suggest that both Mg^{2+} and spermine were adsorbed to the surface of the virus. The adsorbed cations can neutralize the surface of the virus (between 100 and 500 mM $MgCl_2$ or between 0.5 and 1 mM Spermine) and at high enough concentration to overcharge the virus with a net positive charge.

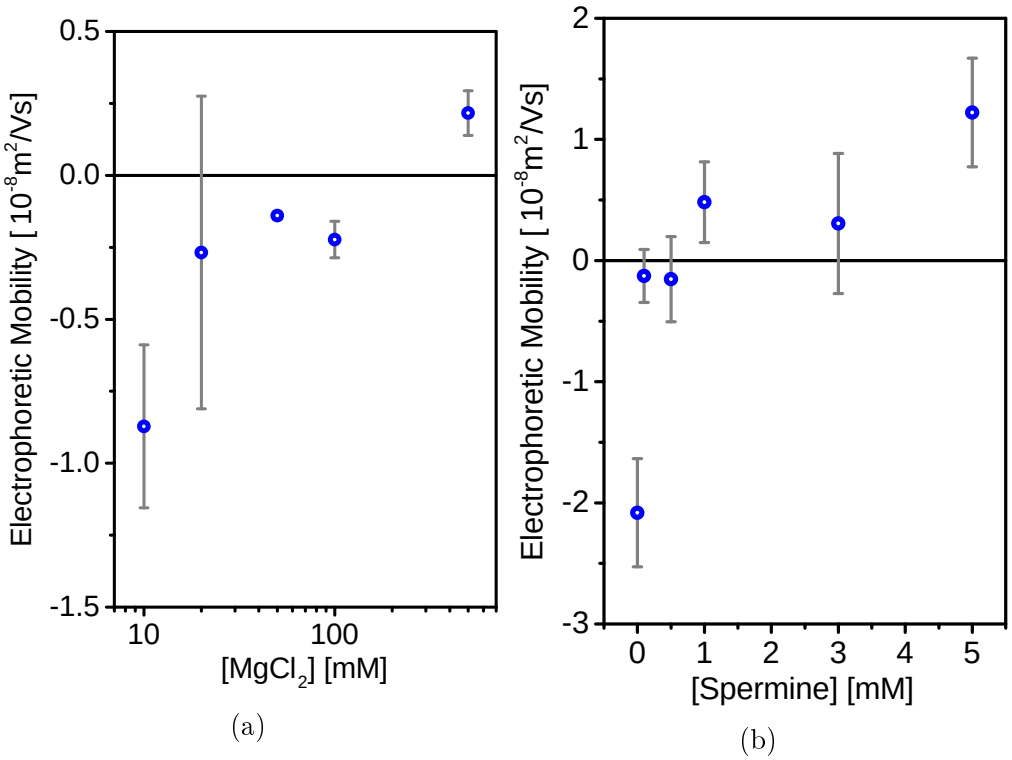

Figure S9: Electrophoretic mobility of wt SV40 as a function of $MgCl_2$ (a) or Spermine (b) concentration. As the salt concentration increased the electrophoretic mobility changed from net negative (in pure water) to net positive. Virus surface charge neutrality was obtained between 100 and 500 mM $MgCl_2$ or between 0.5 and 1 mM Spermine.

5. Free energy for crystallization

Our thermodynamic model suggests that the net free energy change for virus crystallization is given by $\mu\Delta N_{Mg^{2+}}$ (Eq. 11) where μ is the chemical potential in the bulk salt solution and $\Delta N_{Mg^{2+}}$ is effectively the difference between the number of Mg^{2+} cations per virus that are in bridging positions and the number of Mg^{2+} cations that are bound to the soluble virus on the same surface areas as the contact surface in the crystal (Eq. 12). The crystallization first appeared when the size of $\Delta N_{Mg^{2+}}$ was positive enough for the free energy change to overcome the entropy of the virus particles. This result means that the number of adsorbed cations in the bridging positions is more than twice the number of cations in a similar contact area on two soluble viruses (see Eq. 12). This result holds at relatively low coverage fractions. At the higher $MgCl_2$ concentrations, the chemical potential of the cations in the solution is higher and the factor $\Delta N_{Mg^{2+}}$ becomes lower and even negative. In this situation the high chemical potential in the bulk will push the system (virus particle) to a state where the number of possible binding site is maximal, which is the soluble phase. At this point, resolibilization of the crystalline phase was observed. Figure S10 shows the variation in $\Delta N_{Mg^{2+}}$ as a function of $MgCl_2$ concentration, according to our model.

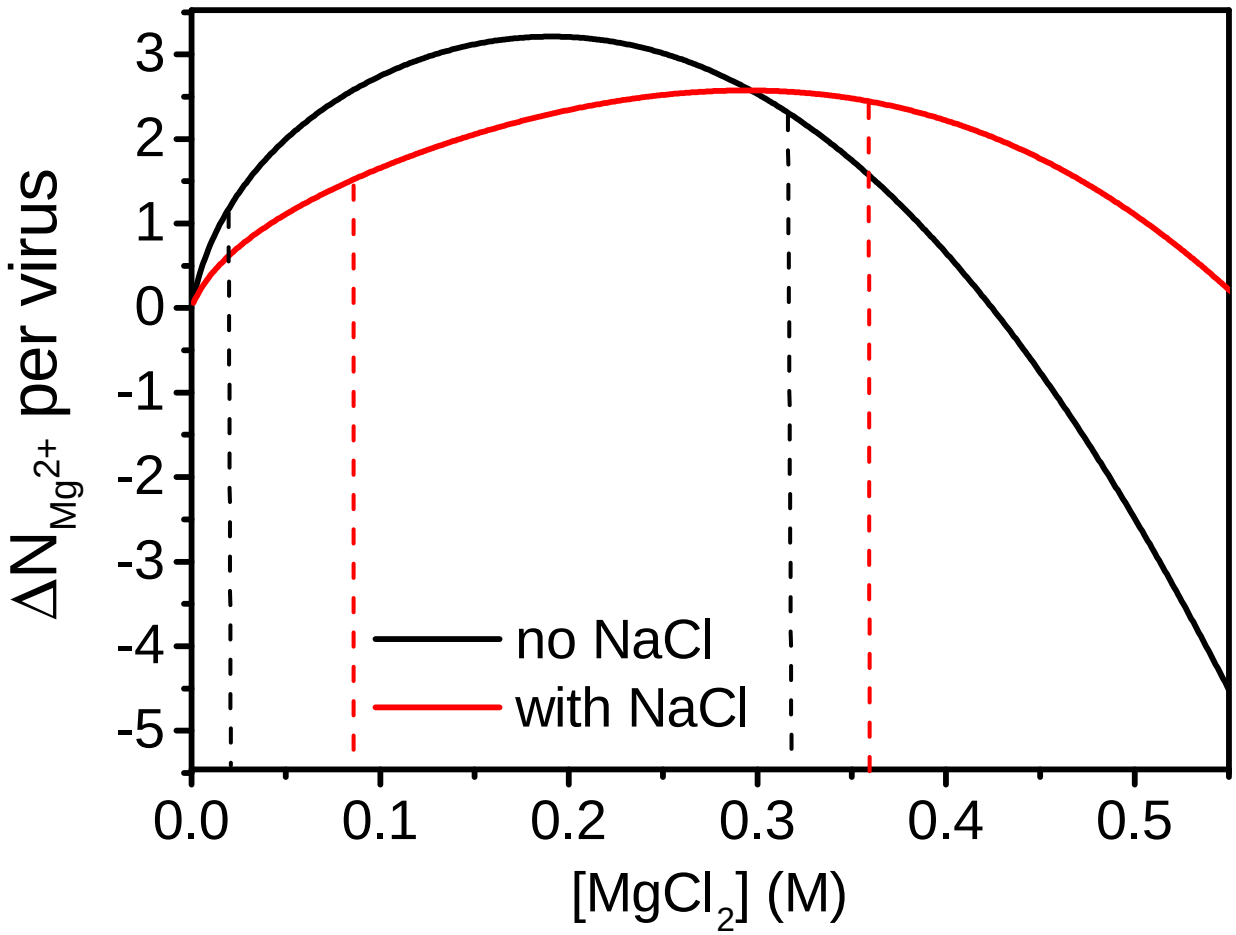

Figure S10: The difference between the number of Mg^{2+} cations per virus that are in a bridging position and the number of Mg^{2+} cations that are bound to the soluble virus ($\Delta N_{Mg^{2+}}$) with or without added NaCl and as a function of the $MgCl_2$ concentration. The dashed vertical lines represent c^* and c^{**} for each system.

References

1. Ben-Nun, T.; Ginsburg, A.; Székely, P.; Raviv, U. X+: a Comprehensive Computationally Accelerated Structure Analysis Tool for Solution X-ray Scattering from Supramolecular Self-Assemblies. *J. Appl. Crystallogr.* **2010**, *43*, 1522–1531.

2. Székely, P.; Ginsburg, A.; Ben-Nun, T.; Raviv, U. Solution X-ray Scattering form Factors of Supramolecular Self-Assembled Structures. *Langmuir* **2010**, *26*, 13110–13129.

3. Saper, G.; Kler, S.; Asor, R.; Oppenheim, A.; Raviv, U.; Harries, D. Effect of Capsid Confinement on the Chromatin Organization of the SV40 Minichromosome. *Nucleic acids Res.* **2012**, 1569–1580.

4. Ben-Nun, T.; Asor, R.; Ginsburg, A.; Raviv, U. Solution X-ray Scattering Form-Factors with Arbitrary Electron Density Profiles and Polydispersity Distributions. *Isr. J. Chem.* **2015**,

5. Bonneté, F.; Finet, S.; Tardieu, A. Second Virial Coefficient: Variations with Lysozyme Crystallization Conditions. *J. Cryst. Growth* **1999**, *196*, 403–414.

6. Ginsburg, A.; Ben-Nun, T.; Asor, R.; Shemesh, A.; Ringel, I.; Raviv, U. Reciprocal Grids: A Hierarchical Algorithm for Computing Solution X-ray Scattering Curves from Supramolecular Complexes at High Resolution. *J. Chem. Inf. Model.* **2016**, *56*, 1518–1527.

7. Als-Nielsen, J.; McMorrow, D. *Elements of Modern X-Ray Physics*; John Wiley & Sons, 2011.

8. Bertin, A.; Mangenot, S.; Renouard, M.; Durand, D.; Livolant, F. Structure and Phase Diagram of Nucleosome Core Particles Aggregated by Multivalent Cations. *Biophys. J.* **2007**, *93*, 3652–3663.

9. De Frutos, M.; Raspaud, E.; Leforestier, A.; Livolant, F. Aggregation of Nucleosomes by Divalent Cations. *Biophys. J.* **2001**, *81*, 1127–1132.

10. Mangenot, S.; Leforestier, A.; Durand, D.; Livolant, F. Phase Diagram of Nucleosome Core Particles. *J. Mol. Biol.* **2003**, *333*, 907–916.

11. Henry, D. C. The Cataphoresis of Suspended Particles. Part I. The Equation of Cataphoresis. *Proc. R. Soc. London, Ser. A* **1931**, *133*, 106–129.

12. Vega-Acosta, J. R.; Cadena-Nava, R. D.; Gelbart, W. M.; Knobler, C. M.; Ruiz-GarcÃŋa, J. Electrophoretic Mobilities of a Viral Capsid, Its Capsid Protein, and Their Relation to Viral Assembly. *J. Phys. Chem. B* **2014**, *118*, 1984–1989, PMID: 24467401.